

# Tomography of Turbulence Strength Based on Scintillation Imaging

Nir Shaul<sup>✉</sup> and Yoav Y. Schechner<sup>✉</sup>

Viterbi Faculty of Electrical and Computers Eng.,  
Technion - Israel Institute of Technology, Haifa, Israel  
nir.shaul@gmail.com , yoav@ee.technion.ac.il

**Abstract.** Developed areas have plenty of artificial light sources. As the stars, they appear to twinkle, i.e., scintillate. This effect is caused by random turbulence. We leverage this phenomenon in order to reconstruct the spatial distribution the turbulence strength (TS). Sensing is passive, using a multi-view camera setup in a city scale. The cameras sense the scintillation of light sources in the scene. The scintillation signal has a linear model of a line integral over the field of TS. Thus, the TS is recovered by linear tomography analysis. Scintillation offers measurements and TS recovery, which are more informative than tomography based on angle-of-arrival (projection distortion) statistics. We present the background and theory of the method. Then, we describe a large field experiment to demonstrate this idea, using distributed imagers. As far as we know, this work is the first to propose reconstruction of a TS horizontal field, using passive optical scintillation measurements.

**Keywords:** Computational photography; Multi-view imaging; Atmospheric remote sensing

## 1 Introduction

A beautiful visual scene is that of twinkling stars. Twinkling is even stronger when observing by the naked eye artificial light sources (bulbs) at a distance. This effect is formally termed *scintillation* [8,24], and it is caused by atmospheric turbulence. Prior computer vision art on turbulence mostly seeks image enhancement [12,25,49], and simulations [34]. However, turbulence *encodes* information about scenes, such as distance to background objects [41,48] and crosswind [1,28].

We deal with sensing of the turbulence itself, specifically the field of turbulence strength (TS). It is important to quantify and model turbulence due to its effect on wind turbine farms [26], meteorology, aviation [39], free space communication and other technologies [10,45]. To quantify TS, the main methods recover a *single* value which averages [41,47] the TS over a single line of sight (LOS). The LOS is between a fixed laser source and fixed detector (a scintillometer), or that of a camera [23,44]. However, the TS generally varies spatially [13]. There are methods that resolve the TS over a LOS, using high definition correlation of objects around the LOS [6,15,27,32,37]. At a laboratory scale, TS can be spatially resolved by active coherent illumination [17] (holography).



**Fig. 1.** Scintillating light sources over Haifa Bay, imaged on a winter evening. [Left] A preliminary capture of a twilight scene consists of lights and landmarks. [Right] Operational imaging optimized for turbulence scintillation sensing. Colors encode processed results: valid measurements are in green; red denotes signals that are either saturated or too dim.

We suggest a method for reconstructing the TS in a wide horizontal field. The sensing is passive, relying on scintillation of bulbs that happen to be in the scene. The bulbs are observed from multiple cameras in a wide breadth of locations and fields of view (FOV). Data analysis is that of linear tomography, i.e., multi-view imaging for volumetric reconstruction. The main idea is that a scintillation index of an observation is linearly related to the spatially varying TS.<sup>1</sup> Our work is related to [3]. In [3], measurement linearly weight TS in a way that is mostly sensitive to air near a camera. However, usually we are interested in remote sensing of TS in a wide, deep domain, rather than the air adjacent to a camera. Our method, in contrast, is most sensitive around the domain core. We therefore yield better sensing of regions that are inaccessible.

The reason for this is that the sensing principle of [3] is temporal geometric distortion, caused by turbulence mainly near the camera. On the other hand, our sensing principle is scintillation, which is mostly affected by air away from a camera and the objects it observes. We provide the theory of this tomographic principle. We further demonstrate it in a city-scale real experiment, which includes a set of cameras dispersed in the domain. This adds-up to other recent work in computer vision, which seeks new ways for sensing of the atmosphere, particularly using new types of tomography [2,16,21,22,40].

## 2 Background on Turbulence

Denote a spatial location in a refractive medium by  $\mathbf{X} = (X, Y, Z)$ . In our case, the medium is air. Uppercase  $Z$  denotes *vertical location* in 3D. Over time  $t$ , the medium changes due to eddies having variable temperatures, pressure and humidity. The eddies are created by winds or local heating sources on the ground. The eddies are chaotic and constitute *turbulence*. The said medium variations

<sup>1</sup> Note that tomography to sense properties of atmospheric scatterers is non-linear in the unknowns [21,22,30,35].

lead to changes in the medium's refractive index, denoted as the unit-less  $n(\mathbf{X}, t)$ . The changes are chaotic, but have established statistics. For temporally stationary turbulence [3], a *structure function* [20,41] is defined by

$$\mathcal{D}_n(\mathbf{X}_1, \mathbf{X}_2) = \langle [n(\mathbf{X}_1, t) - n(\mathbf{X}_2, t)]^2 \rangle_t \quad (1)$$

for any two points  $\mathbf{X}_1, \mathbf{X}_2$  in the medium. Typical times scales of turbulence in air are 1 sec to 1 hour, corresponding to length scales from 1 mm up to the order of 1 km. Within these scales,  $\mathcal{D}_n$  is spatially wide-sense-stationary, according to Kolmogorov [18,19]. Let us approximate the structure function as space-invariant, depending only on the distance  $\rho = \|\mathbf{X}_1 - \mathbf{X}_2\|$ , in units of meters. Then

$$\mathcal{D}_n(\rho) = C_n^2 \rho^{2/3}. \quad (2)$$

Here  $C_n^2$  is termed the refractive index *structure constant* [20,41]. The units of  $C_n^2$  are  $m^{-2/3}$ . The structure constant is non-negative and has typical values in the range  $10^{-17}m^{-2/3}$  to  $10^{-13}m^{-2/3}$ .

The TS is quantified by  $C_n^2$ . Suppose  $C_n^2 = 0$  in Eq. (2). Then Eq. (1) means that the refractive index is spatially uniform, which occurs when the medium is still. The higher  $C_n^2$  is, the higher the spatiotemporal variability of the refractive index. This leads to observable optical effects [13]. In large scales, some regions are more turbulent than others, due to spatial variations of temperature gradients and winds. Thus we denote TS by  $C_n^2(\mathbf{X})$ . Locally, nature it is quasi-stationary, allowing the use of space-invariant correlations as Eq. (2). Indeed, the form  $C_n^2(\mathbf{X})$  is prevalent in prior art [15,32], including theory [20,38].

### Vertical vs. Horizontal Imaging

There is a clear distinction between imaging of celestial objects (e.g., stars) and low-altitude objects. The atmosphere is thin: air pressure falls to half that of sea-level at 5km. Moreover, local topographic features (which affect wind) and sources of temperature gradients and moisture are mainly on the ground. Thus turbulence effects are strongest at very low altitudes. In a vertical observation of a celestial object, the LOS is mostly [27] affected by the lowest 3km (see Fig. 2). The situation is very different [27,46] when observing objects near ground (horizontal views). Then, the entire LOS passes through the densest air, rich in turbulence sources. Moreover, horizontal paths can extend far beyond 3km. Hence, horizontal imaging easily expresses strong visual effects of turbulence.

One of visual effects of turbulence is termed *Seeing*. In this effect, random refraction perturbs the angle of arrival (AOA) of a ray from an object to the camera [33]. Thus, the LOS of each pixel wiggles, creating spatiotemporal geometric distortions in image sequences. For an object at distance  $L$  and a camera having a lens aperture diameter  $D$ , the AOA of a LOS has variance given by

$$\sigma_{\text{AOA}}^2 = 2.914D^{-1/3} \int_0^L C_n^2[\mathbf{X}(z)]w_{\text{AOA}}(z|L)dz, \quad \mathbf{X} \in \text{LOS} \quad (3)$$

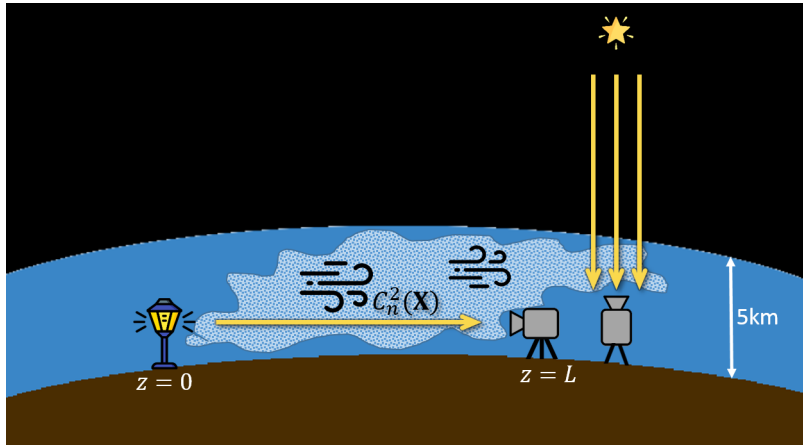


**Fig. 2.** Vertical and horizontal turbulence paths. For vertical paths, approximately 60% of the turbulence is located 3km near the sensor [27], and the propagation model is that of a collimated beam (plane wave). In horizontal imaging, turbulence can be strong all along the LOS, and the propagation model is that of a point source (spherical wave).

where

$$w_{\text{AOA}}(z|L) = \left(\frac{z}{L}\right)^{5/3}. \quad (4)$$

Note that  $z \in [0, L]$  is a *location parameter* along a LOS. Here  $z = 0$  corresponds to the object location, while the camera is at  $z = L$  (Fig. 2). The term  $w_{\text{AOA}}(z|L)$  weights the contribution of  $C_n^2[\mathbf{X}(z)]$  along the LOS. From Eq. (4), clearly, the contribution is maximal by a turbulent air parcel right near the camera lens. The farther the turbulent air parcel (lower  $z$ ), the smaller is its effect on  $\sigma_{\text{AOA}}^2$ .

Another visual effects of turbulence is termed *Scintillation*. It is the reason that stars twinkle. Similarly, it is the reason that distant bulbs on horizontal paths twinkle. In scintillation, the measured light intensity fluctuates. We provide more details about this effect in Sec. 3.

### 3 Scintillation by Turbulence

There are several theories of scintillation, based on different approximations of light propagation [29,31]. Here we provide an intuitive illustration of how a turbulent medium creates twinkling, in a camera observing a single isotropic point source. Consider a very simplified case, where an air parcel has a shape of a lens, and its refractive index is slightly lower than that of calm steady air. Then, the air parcel acts as a very weak diverging lens (Fig. 3).

If the air parcel is adjacent to the camera lens ( $z = L$ ), then it has a negligible effect on the light flux gathered by the camera. A similar outcome occurs if the air parcel is adjacent to the isotropic point object ( $z = 0$ ). As a result, no matter what is the random refractive index of the air parcel, it does not change

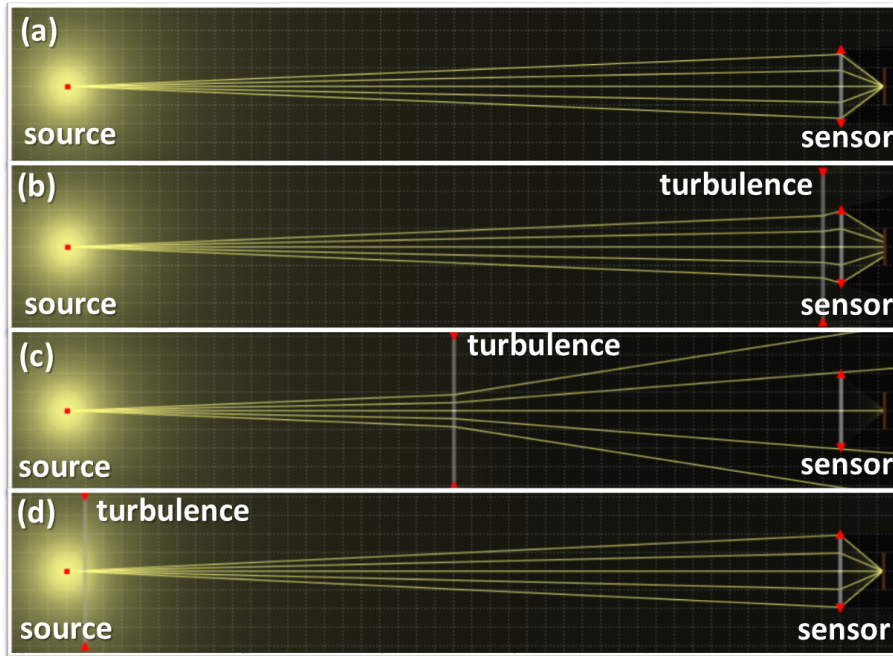


**Fig. 3.** Ray tracing simulation, modeling turbulence phenomena as defocusing by a lens. The influence of the turbulence is minor if it is located close to the sensor **(b)** or to the point source **(d)**. The influence becomes major while located in the middle **(c)**. Based on a ray-tracing simulator [50].

the measured intensity in these two cases. However, if the air parcel is at the center of the LOS, ( $z = L/2$ ), it has a significant effect: some light rays miss the camera aperture, leading to loss of light gathered by the camera. Because the air-parcel has a random refractive index, the loss of gathered light power is random. This leads to observed scintillation. In analogy to Eqs. (3,4), we thus expect that in scintillation<sup>2</sup> of an isotropic source (marked  $\bullet$ ), there is a weight of  $C_n^2[\mathbf{X}(z)]$  along a LOS, which satisfies

$$w_{\text{scint}}^{\bullet}(z = 0|L) = 0, \quad w_{\text{scint}}^{\bullet}(z = L|L) = 0, \quad L/2 = \arg \max_z w_{\text{scint}}^{\bullet}(z|L). \quad (5)$$

An isotropic light source emits a spherical wave. Rigorous wave-optics analysis of scintillation of a spherical wave yields the following result. Let the intensity observed by the camera at time  $t$  be  $I(t)$ . Its expectation value is  $\langle I(t) \rangle_t$ . Define

<sup>2</sup> From the illustration, despite beam spread caused by turbulence, if the camera lens is large enough, the lens gathers the light power as in non-turbulent air. This inhibits the scintillation signal, and termed *aperture filtering*. In practice, the aperture filters scintillation if  $D > 5\text{cm}$ . In our work, this is negligible because  $D < 5\text{cm}$ .

a unit-less normalized variance by

$$\sigma_1^2 = \left\langle \left[ \frac{I - \langle I(t) \rangle_t}{\langle I(t) \rangle_t} \right]^2 \right\rangle_t = \frac{\langle I^2(t) \rangle_t - [\langle I(t) \rangle_t]^2}{[\langle I(t) \rangle_t]^2} = \frac{\langle I^2(t) \rangle_t}{[\langle I(t) \rangle_t]^2} - 1. \quad (6)$$

In our context,  $\sigma_1^2$  is termed a *scintillation index*. For a spherical wave having wavelength  $\lambda$  propagating in a turbulent medium, the scintillation index is modelled [20,24,38] by

$$\sigma_{1\bullet}^2 = 2.24 \left( \frac{2\pi}{\lambda} \right)^{7/6} \int_0^L C_n^2[\mathbf{X}(z)] w_{\text{scint}}^\bullet(z|L) dz, \quad \mathbf{X} \in \text{LOS} \quad (7)$$

where

$$w_{\text{scint}}^\bullet(z|L) = (L - z)^{5/6} \left( \frac{z}{L} \right)^{5/6}. \quad (8)$$

Note that Eq. (8) is consistent with Eq. (5).

There is an additional model of scintillation, where the object is a star [5,7,27], far away from the turbulent medium, observed vertically from Earth (Fig. 2), or a laser-based scintillometer [42]. Each can be approximated as a plane wave source, marked  $\parallel$ . Then, the scintillation index is modelled by

$$\sigma_{1\parallel}^2 = 2.24 \left( \frac{2\pi}{\lambda} \right)^{7/6} \int_0^L C_n^2[\mathbf{X}(z)] w_{\text{scint}}^\parallel(z|L) dz, \quad \mathbf{X} \in \text{LOS} \quad (9)$$

where

$$w_{\text{scint}}^\parallel(z|L) = (L - z)^{5/6}. \quad (10)$$

The weight functions  $w_{\text{AOA}}(z|L)$ ,  $w_{\text{scint}}^\bullet(z|L)$ ,  $w_{\text{scint}}^\parallel(z|L)$  are plotted in Fig. 4. According to Ref. [8], in a weak scintillation regime,  $\sigma_1^2 < 0.2$ , while  $I(t)$  is sampled from approximately a log normal distribution. In a very weak regime,  $\sigma_1^2 < 0.1$ , while  $I(t)$  is sampled approximately from a normal distribution.

## 4 TS Tomography From Scintillation

We formalize an inverse problem, of reconstructing  $C_n^2$  from scintillation measurements of point sources. The formulation is that of a linear tomography problem. As seen in Eq. (7), over a single LOS, the scintillation index is a linear (weighted) integral of  $C_n^2(\mathbf{X})$ . Linear path integrals are the basis of linear tomography as used in medical imaging.

Analogously, we formulate TS tomography based on scintillation of point sources at horizontal views. As in medical imaging, we need multi-view projections. Then, different LOSs yield a set of independent linear equations as (7), modeling how the unknown field  $C_n^2(\mathbf{X})$  leads to the set of measured  $\sigma_1^2$ .

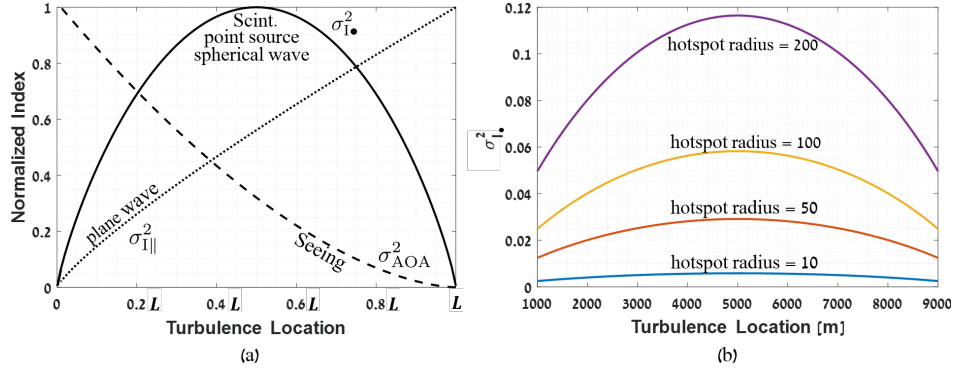


**Fig. 4.** (a) Spherical wave, plane wave, and AOA theoretical Weights. (b) Simulation results, for a set of hot-spot locations and radii. Here  $C_n^2 = 1e^{-15} m^{-2/3}$ . The sensor and source are located at  $X = 0$  and  $X = 10$  km, respectively.

Empirically, Eq. (6) uses a sequence of images. Each image is affected by image noise, including photon noise. This aspect needs to be accounted for. Let  $p$  denote a specific pixel observing a point object (bulb)  $\mathbf{O}$  from a specific viewpoint. Without turbulence, in a lab, the variance of imaging noise ( $\text{VAR}_{\text{noise}}$ ) can be calibrated per expected graylevel  $\langle I(t) \rangle_t$ . Imaging noise is independent of turbulence-induced scintillation, whose variance is  $\text{VAR}_{\text{scint}}(p)$ . Therefore, the empirical variance  $\text{VAR}_{\text{data}}$  of the measured intensity of  $\mathbf{O}$  satisfies

$$\text{VAR}_{\text{data}}(p) = \text{VAR}_{\text{scint}}(p) + \text{VAR}_{\text{noise}} . \quad (11)$$

Therefore, from Eqs. (6,7,11), a datum at  $p$  is

$$y(p) \equiv \sigma_{I\bullet}^2(p) = \frac{\text{VAR}_{\text{data}}(p) - \text{VAR}_{\text{noise}}}{[\langle I(p, t) \rangle_t]^2} . \quad (12)$$

Now, the continuous model of Eqs. (7,8) is discretized. The domain is divided into a set of  $N_{\text{voxels}}$  voxels,  $\{V_k\}_{k=1}^{N_{\text{voxels}}}$ . TS is approximated as a constant within each voxel. We follow some of the notations of Ref. [3]. Pixel  $p$  observes object  $\mathbf{O}$  through  $\text{LOS}_p$  (Fig. 5). As  $p$  relates to a specific viewpoint (camera) which observes  $\mathbf{O}$ , the distance of the camera from  $\mathbf{O}$  is denoted  $L(p)$ . The intersection of  $\text{LOS}_p$  with voxel  $V_k$  is denoted  $\Psi_{p,k} \equiv \text{LOS}_p \cap V_k$ . If  $\text{LOS}_p$  does not intersect voxel  $V_k$ , then  $\Psi_{p,k}$  is empty. The intersection is a line segment between two points  $s_{p,k}^{\min}, s_{p,k}^{\max}$ , defined by

$$s_{p,k}^{\min} = \min_{\mathbf{X} \in \Psi_{p,k}} \|\mathbf{X} - \mathbf{O}\| \quad s_{p,k}^{\max} = \max_{\mathbf{X} \in \Psi_{p,k}} \|\mathbf{X} - \mathbf{O}\| . \quad (13)$$

Using Eq. (8), define

$$a(p, k) = 2.24 \left( \frac{2\pi}{\lambda} \right)^{7/6} \int_{s_{p,k}^{\min}}^{s_{p,k}^{\max}} w_{\text{scint}}^{\bullet}[z|L(p)] dz . \quad (14)$$

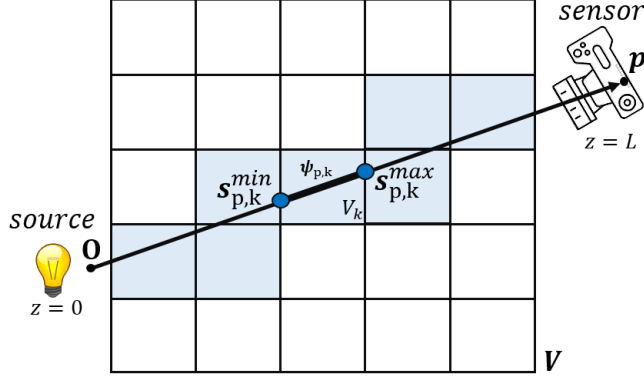


**Fig. 5.** Line of sight ray-voxel intersection. Points  $s_{p,k}^{\min}$  and  $s_{p,k}^{\max}$  are the intersection points of the ray with voxel  $V_k$ . We used the ray tracing algorithm of [4].

There is a closed form for the integral in Eq. (14), using the hypergeometric [14] function  ${}_2F_1$

$$\int_{s_{p,k}^{\min}}^{s_{p,k}^{\max}} w_{\text{scint}}^{\bullet}[z|L(p)] dz = \frac{6z[L(p) - z]^{5/6} \left[ \frac{z}{L(p)} \right]^{5/6} {}_2F_1\left(-\frac{5}{6}, \frac{11}{6}; \frac{17}{6}; \frac{z}{L(p)}\right)}{11[1 - \frac{z}{L(p)}]^{5/6}} \Bigg|_{s_{p,k}^{\min}}^{s_{p,k}^{\max}}, \quad (15)$$

where

$${}_2F_1(\alpha, \beta; \gamma; \xi) = \sum_{m=0}^{\infty} \frac{(\alpha)_m (\beta)_m}{(\gamma)_m} \frac{\xi^m}{m!}. \quad (16)$$

Because TS is approximated as a constant within each voxel  $k$ , Eq. (7) is discretized to a sum:

$$\sigma_{\mathbf{I}_{\bullet}}^2(p) \approx \sum_{\Psi_{p,k} \neq \emptyset} a(p, k) C_n^2(k). \quad (17)$$

This sum can be approximated also using linear interpolation.

The total number of pixels in all viewpoints is  $N_{\text{pixels}}$ . Define a  $N_{\text{pixels}} \times N_{\text{voxels}}$  matrix  $\mathbf{A}$ , whose element  $(p, k)$  is

$$A(p, k) = \begin{cases} 0 & \text{if } \Psi_{p,q} = \emptyset \\ a(p, k) & \text{otherwise} \end{cases}. \quad (18)$$

Based on Eq. (12), concatenate the values  $y(p)$  for all  $p$  into a column vector  $\mathbf{y}$ . Concatenate the variables  $C_n^2(k)$  for all  $k$  into a column vector  $\mathbf{c}$ . Then Eq. (17) has the form

$$\mathbf{y} \approx \mathbf{A} \mathbf{c}. \quad (19)$$



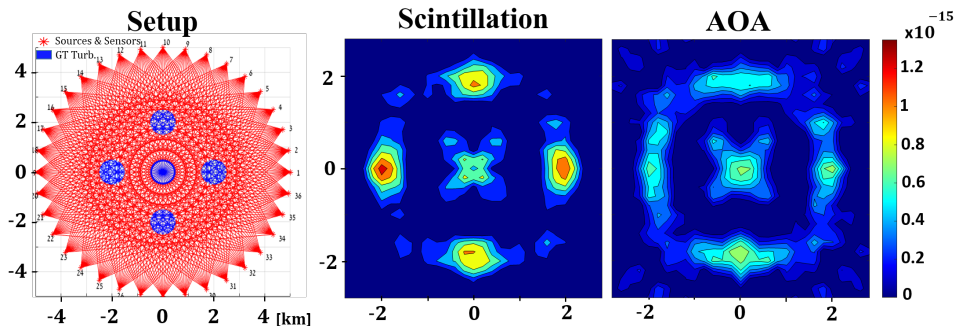


**Fig. 6.** [Left] Simulation of a uniform radial topology of sources and sensors. Each sensor acts as a source for the opposite sensors. [Middle] Scintillation-based TS tomography result (NRMSE = 0.158). Notice all five TS blobs were reconstructed. [Right] Results of AOA-based TS tomography (NRMSE = 0.217).

The tomographic inverse problem can then be solved using

$$\hat{\mathbf{c}} = \arg \min_{\mathbf{c}} \left\{ \|\mathbf{y} - \mathbf{A}\mathbf{c}\|^2 + \mu R(\mathbf{c}) \right\} \quad s.t. \quad \mathbf{c} \geq \mathbf{0}. \quad (20)$$

Here  $\mu$  is a regularization parameter and  $R(\mathbf{c})$  is a regularization term. Here we chose a spatial smoothness prior  $R(\mathbf{c}) = \|\nabla^2 \mathbf{c}\|^2$  as an example. We use the simultaneous algebraic reconstruction technique (SART) [11] as a solver. Other priors can also be used.

## 5 Simulation

Consider Fig. 6. A simulated circular domain has a diameter of 10km. It is surrounded by 36 cameras. Each camera location has a bulb, to be observed by the other cameras. Each camera has a fixed FOV of  $80^\circ$ . A camera has 15 pixels, each observing a bulb. Thus  $N_{\text{pix}} = 540$ . The domain includes five turbulent circular hot-spots, at and around the domain center, Each hot-spot has a 500m radius and TS  $C_n^2 = 10^{-15} m^{-2/3}$ .

Each pixel has full-well of 3000 photoelectrons and 8-bit quantization, i.e., the expected number of photoelectrons per graylevel is 11.8. Using these specifications, each noisy measurement is drawn from a Poisson distribution of photoelectrons, and then quantized. A sequence of 1000 frames was then used for tomography. From this sequence, we estimated both  $\sigma_{\text{AOA}}^2(p)$  and  $\sigma_{\text{I}\bullet}^2(p)$ , for each pixel  $p$ . The values of  $\sigma_{\text{AOA}}^2$  are used to run the method of Ref. [3], to which we compare. Fig 6 shows our result, in comparison to that obtained by the principle of Ref. [3]. In Fig. 7 we simulate a scene of one blob, in a sensors' configuration as that of the field experiment (Sec. 6).

We studied how  $N_{\text{pix}}$  affects the results. We changed the number of cameras in the range 9 to 88, but keeping the FOV of each at  $80^\circ$ . Each camera has a

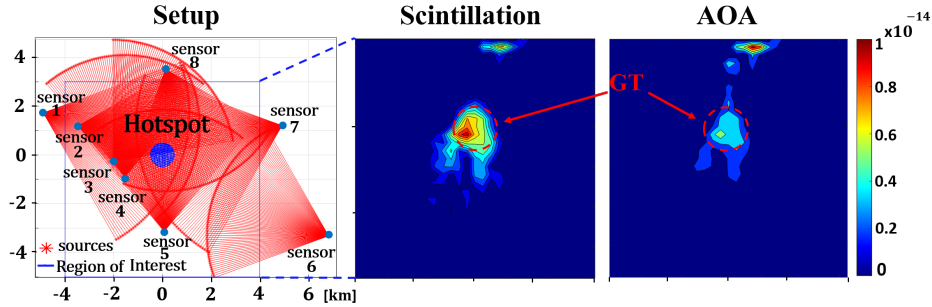


Fig. 7. TS simulated recovery. Cameras are placed as in the field experiment.

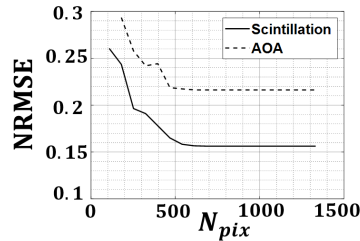


Fig. 8. TS Reconstruction NRMSE over  $N_{pix}$ .

bulb to be observed by the other cameras. This way  $N_{pix}$  varies in the range [108, 1332]. Results of the estimated  $\hat{C}_n^2$  are quantitatively compared to the true  $C_n^2$  using the normalized root mean square error (NRMSE),

$$\text{NRMSE} = \frac{\sqrt{\langle [\hat{C}_n^2(k) - C_n^2(k)]^2 \rangle_k}}{\max_k C_n^2(k)}, \quad (21)$$

where  $k$  is the voxel index. The results are plotted in Fig. 8.

We also checked the influence of the distance of the hot-spots from the camera ring, and the radius of each hot-spot. The results appear in Fig. 4b. The dependency on distance is consistent with the theory [24]. Note that the scintillation index is in the range  $0 \leq \sigma_{I_\bullet}^2(p) \leq 0.2$ .

## 6 Field Experiment

Turbulence effects typically require very long ranges. Hence, we conducted a field experiment in a greater-city scale, at the Haifa Bay, Israel. This is a domain which is about 10km across. The experiment included the following elements:

*Building imaging systems.* We need to simultaneously image a field of a large scale, yet with high angular resolution, in order to resolve individual bulbs at large distances. For this purpose, we custom-built a set of untethered imaging



**Fig. 9.** [Left] Sample images from the outdoor experiment. [Right] A custom-built imager. It consists of an industrial camera, a C-mount lens, a raspberry-pi controller and a motorized pan and tilt head.

**Table 1.** Components of the imaging system

Component	Model	Spec.
Machine Vision Camera	IDS UI-3480LE-M-G	2560x1920, $2.2\mu\text{m}^2$
Lens	Fujinon HF75SA-1	$f/11$ , $f = 75\text{mm}$
Controller	Raspberry Pi 4B	8 GB RAM, WiFi
Motorized Pan & Tilt Head	Bescor MP-101	$0\text{-}340^\circ$ , $\pm 15^\circ$
Power Bank	Xiaomi Redmi 18W	20,000mAh, 3.6A
Housing	Nisko T2 IP55	90x150x80 mm
Cellular Modem	Boon	WiFi-cellular

systems (see Fig. 9). Each integrates power, embedded computing, communications, electro-mechanics, a camera, a lens and a dedicated software.

Table 1 lists hardware components. An industrial machine vision camera provides radiometric reliability. The lens provides high angular resolution ( $0.035$  mrad/pixel), but limits the FOV ( $4.301^\circ$ ). So, a motorized pan-tilt unit head scans the FOV. A baffle attached to the lens reduces stray light from peripheral bulbs. Remote control and verification is by cellular communication. The camera, pan-tilt-unit and communications are automatically controlled by a raspberry-pi controller running the software. Scintillation degrades by *aperture filtering* [9]. So, a small aperture is used ( $f/11$ ). Light bulbs flicker due to alternating-current (AC) in the power grid [36]. This flicker may overwhelm the scintillation signal. This disturbance is filtered out using a 80ms exposure time (an integer multiple of the period of the grid's AC). At 80ms, the exposure of distant bulbs was sufficient. In each view angle, 50 frames were acquired, for latter processing. From Eq. (8), wavelengths scale the scintillation index, but add no information regarding the TS. Night capture requires maximal light sensitivity. So, no spectral filter was added to the panchromatic camera. The sensitivity of IDS UI-3480LE-M-G peaks at  $\lambda = 500\text{nm}$ , which we used in (14).

*Waiting for a feasible experiment opportunity:* a night having no rain, fog or pandemic lock-downs, while a team is available to cover the region.

*Simultaneous imaging by a team.* At dusk, natural lighting makes the landscape visible in conjunction to the lit-up bulbs. This enables identification and localization of each bulb of interest in the FOV. On 02/02/2022, a team of volunteers went to eight viewpoint locations, setting an untethered imaging system in each. Preliminary imaging started at dusk (5:15PM local time), for bulb localization. Then, at night (5:45PM to 6:10PM), imaging of bulb scintillation took place. We make the the raw data, codes and system design of the field experiment publicly available in: <https://github.com/nirshaul/ScintillationTomography>

*Sensor calibration:* The IDS UI-3480LE-M-G is radiometrically linear. We did not need intrinsic geometric calibration: any bulb we used in  $p$  was registered to a specific LOS by recognizing this bulb on a landmark in our known domain. Nevertheless we calibrated the focal length by observing the pixel coordinates of several recognizable bulbs in the FOV, while knowing their corresponding LOS (thus relative LOS angles) in the real world.

*Image analysis* included several steps:

- (a) Filtering out all bulbs whose scintillation approached or reached the graylevel saturation level, or those who were too weak (marked as red in Fig. 1).
- (b) Bulbs appear as blobs. The intensity of a bulb was estimated by summing  $I$  in each blob. Using  $I(p, t)$ , potential sources are mapped by  $B(p) \equiv 1$  if  $[\max_t I(p, t)] > 20$ , else  $B(p) = 0$ . MATLAB's `bwconncomp` finds connected components in  $B(p)$ : each is an individual blob, where  $I(p, t)$  is spatially integrated. This yields a time sequence (for 50 frames), per blob. When possible, longer sequences are measured.
- (c) Per spatially-integrated bulb,  $\langle I(t) \rangle_t, \langle I^2(t) \rangle_t$  are calculated, leading to (6).
- (d) Each bulb of interest was registered to ground location coordinates. This was done using dusk images and maps of the region.
- (e) The GPS coordinates of each viewpoint defined the LOS to each bulb. In total, we marked 327 LOSs, each with a corresponding  $\sigma_1^2$  value (Fig. 10).
- (f) In our outdoor field, viewpoints and the ground vary vertically by 50m at most, over a horizontal span of 6-12km. So, we do not attempt vertical resolution. The domain was divided horizontally to  $15 \times 27$  voxels, each 500m long. This way, the number of unknowns is comparable the 327 measured LOSs to recognized landmarks. The voxel-size order of magnitude is consistent with prior art (200m in [32]; 600m in [3]). We ran Eqs. (13-20), using  $\mu = 0.3$ .

The result is shown in Fig. 12. Major TS hotspots are consistent with major heavy-industry plants, specifically oil refineries having a cluster of chimneys and a fertilizer plant. There was medium-TS in an industrial suburban area, and very low TS in vegetated regions. The maximum in TS values were  $2.3e^{-16}m^{-2/3}$  and

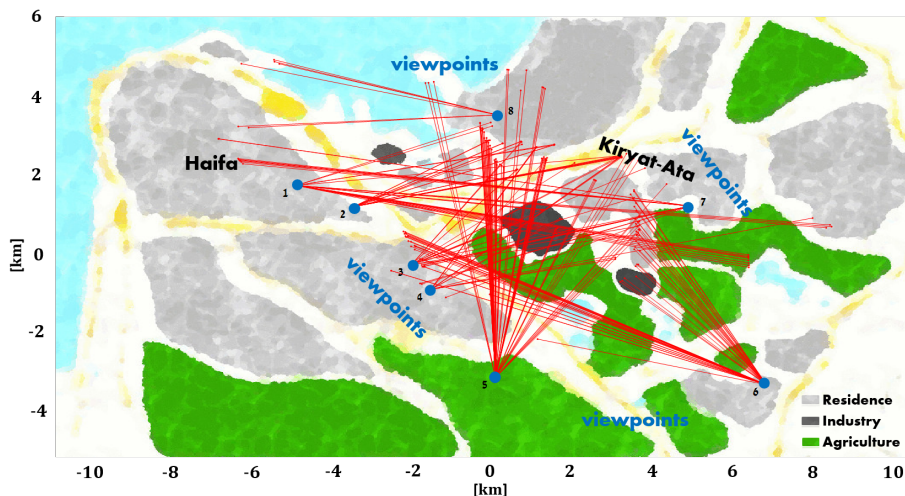


**Fig. 10.** Outdoor experiment setup: Eight viewpoints spread around Haifa Bay. Several dozens of lines of sight measurements were associated to each sensor.

$2.45e^{-16}m^{-2/3}$  (at the refineries and the Kiryat-Ata town, respectively). These values are consistent with typical values in a winter evening [43,46].

## 7 Discussion

We present a novel approach for resolving turbulence strength spatially. We rely on the phenomenon of scintillating point light sources. As this approach is based on passive imaging using a basic machine vision tools, it can be easily utilized for a wide area of interests and applications.

The analysis and the experiment here were geared to night-time. Nevertheless, there is an adaptation of scintillation imaging for daytime [48]. This can thus enable our tomographic approach to work in daytime. We believe that far better resolution can be obtained *using the same video data*, if many more LOSs are analyzed. This requires computer vision methods for automatically finding correspondences of solitude bulbs observed at night from very different multiple views, and registering them to the topography. Hence the TS problem can stimulate further computer vision studies.

In medical CT, there is a missing cone (MC) of frequencies, which is the *null subspace* of multi-angular linear projection *across the domain*. TS-by-scintillation may have a null space too, which is fascinating to explore in future work. It is different from medical MC, because our LOSs can begin/end arbitrarily *inside the domain* (to bulbs), and because of  $w_{\text{scint}}^{\bullet}$ .



**Fig. 11.** Sample images from the outdoor experiment. These images from multiple viewpoints were collected as preliminary data. At twilight, we thus capture light sources and landmarks, for registration.

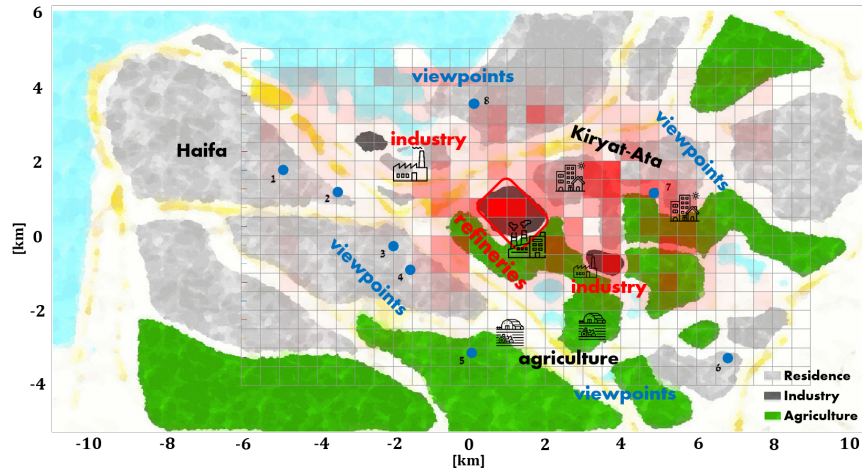


**Fig. 12.** The estimated TS parameter  $C_2^\alpha$ , shown in a 2D map overlaid with regional places of interest. Deep-red areas represent high values, while unsaturated red areas represent low values. Notice the hottest spot is located at the oil refineries.

## Acknowledgments

We thank Uri, Ofra, Dor, Dvir and Inbar Shaul, Roi Ronen, Alon Preger, Haran Man, Vadim Holodovsky and Chanoch Kalifa for participating in the field experiment. Yoav Schechner is the Mark and Diane Seiden Chair in Science at the Technion. He is a Landau Fellow - supported by the Taub Foundation. His work was conducted in the Ollendorff Minerva Center. Minvera is funded through the BMBF. This project has received funding from the European Research Council (ERC) under the European Union's Horizon 2020 research and innovation program (CloudCT, grant agreement No. 810370).

## References


1. Afanasiev, A.L., Banakh, V.A., Rostov, A.P.: Crosswind Measurements From Image Flutter of Remote Objects. In: International Symposium on Atmospheric and Ocean Optics: Atmospheric Physics. vol. 9292, p. 929237 (2014)
2. Aides, A., Schechner, Y.Y., Holodovsky, V., Garay, M.J., Davis, A.B.: Multi Sky-View 3D Aerosol Distribution Recovery. *Optics Express* (2013)
3. Alterman, M., Schechner, Y.Y., Vo, M., Narasimhan, S.G.: Passive Tomography of Turbulence Strength. In: ECCV. Springer (2014)
4. Amanatides, J., Woo, A.: A Fast Voxel Traversal Algorithm for Ray Tracing. *Eurographics* **87**(3), 3–10 (1987)
5. Andrews, L.C., Phillips, R.L., Young, C.Y.: Laser Beam Scintillation with Applications. In: Laser Beam Scintillation with Applications, chap. 3. SPIE (2009)
6. Campbell, M.: Atmospheric turbulence and its influence on adaptive optics (2009)
7. Dravins, D., Lindegren, L., Mezey, E., Young, A.T.: Atmospheric Intensity Scintillation of Stars. II. Dependence on Optical Wavelength. *Publications of the Astronomical Society of the Pacific* **109**, 725 (1997)
8. Dravins, D., Lindegren, L., Mezey, E., Young, A.T.: Atmospheric Intensity Scintillation of Stars. I. Statistical Distributions and Temporal Properties. *Publications of the Astronomical Society of the Pacific* **109**, 173 (1997)
9. Dravins, D., Lindegren, L., Mezey, E., Young, A.T.: Atmospheric Intensity Scintillation of Stars. III. Effects for Different Telescope Apertures: Erratum. *Publications of the Astronomical Society of the Pacific* **110**(751) (1998)
10. Fedorovich, E., Rotunno, R., Stevens, B.: Atmospheric Turbulence and Mesoscale Meteorology. Cambridge University Press (2004)
11. Hansen, P.C., Saxild-Hansen, M.: AIR Tools MATLAB Package of Algebraic Iterative Reconstruction Methods. *J. Comput. Appl. Math.* (2012)
12. He, R., Wang, Z., Fan, Y., Feng, D.: Atmospheric turbulence mitigation based on turbulence extraction. In: IEEE ICASSP (2016)
13. Holtslag, A.A.: Atmospheric Turbulence. In: Meyers, R.A. (ed.) *Encyclopedia of Physical Science and Technology*, vol. 11. Academic Press, New York, third edit edn. (2003)
14. Inc., W.R.: Wolfram Alpha, <https://www.wolframalpha.com/>, accessed: 03/2022
15. Johnston, R.A., Woode, N.J., Reavell, F.C., Bernhardt, M., Dainty, C.: Horizontal Scintillation Detection and Ranging Cn<sup>2</sup>(z) Estimation. *Applied Optics* **42** (2003)
16. Karypidou, S., Georgousis, I., Papakostas, G.A.: Computer Vision for Astronomical Image Analysis. In: IEEE PIC (2021)
17. Klee, A., Thurman, S.T., Alley, T.: Digital Holographic Tomography for Path-Resolved Turbulence Measurements. In: Dolne, J.J., Spencer, M.F. (eds.) *Unconventional Imaging and Adaptive Optics 2021*. SPIE (2021)
18. Kolmogorov, A.N.: Dissipation of Energy in Locally Isotropic Turbulence. In: *Dokl. Akad. Nauk SSSR*. vol. 32, pp. 16–18 (1941)
19. Kolmogorov, A.N.: The Local Structure of Turbulence in Incompressible Viscous Fluid for Very Large Reynolds Numbers. In: *Dokl. Akad. Nauk SSSR* (1941)
20. Kopeika, N.: *A System Engineering Approach to Imaging*. SPIE Press (1998)
21. Levis, A., Davis, A.B., Loveridge, J.R., Schechner, Y.Y.: 3D Cloud Tomography and Droplet Size Retrieval from Multi-Angle Polarimetric Imaging of Scattered Sunlight from Above. In: *Polarization Science and Remote Sensing X*. SPIE (2021)
22. Loeub, T., Levis, A., Holodovsky, V., Schechner, Y.Y.: Monotonicity Prior for Cloud Tomography. In: ECCV. Springer (2020)

23. McKechnie, T.S.: General Theory of Light Propagation and Imaging Through the Atmosphere, Springer Series in Optical Sciences, vol. 196. Springer, Cham (2015)
24. Meijninger, W.M.L.: Surface Fluxes over Natural Landscapes using Scintillometry. Ph.D. thesis, Wageningen university (2003)
25. Nair, N.G., Patel, V.M.: Confidence guided network for atmospheric turbulence mitigation. In: IEEE ICIP (2021)
26. Oberlack, M., Peinke, J., Talamelli, A., Castillo, L., Hölling, M.: Progress in Turbulence Wind Energy IV. In: Proc. iTi Conf. in Turbulence (2010)
27. Osborn, J., Wilson, R.W., Sarazin, M., Butterley, T., Chacón, A., Derie, F., Farley, O.J., Haubois, X., Laidlaw, D., LeLouarn, M., Masciadri, E., Milli, J., Navarrete, J., Townson, M.J.: Optical Turbulence Profiling with Stereo-SCIDAR for VLT and ELT. *MNRAS* **478**(1), 825–834 (2018)
28. Porat, O., Shapira, J.: Crosswind sensing from optical-turbulence-induced fluctuations measured by a video camera. *Applied Optics* **49**(28), 5236–5244 (2010)
29. Rino, C.: The Theory of Scintillation with Applications in Remote Sensing. John Wiley & Sons (2011)
30. Ronen, R., Schechner, Y.Y., Eytan, E.: 4D Cloud Scattering Tomography. In: Proc. ICCV (2021)
31. Sasiela, R.J.: Electromagnetic Wave Propagation in Turbulence: Evaluation and Application of Mellin Transforms: Second edition. SPIE Press (2007)
32. Sauvage, C., Robert, C., Mugnier, L.M., Conan, J.M., Cohard, J.M., Nguyen, K.L., Irvine, M., Lagouarde, J.P.: Near Ground Horizontal High Resolution Cn2 Profiling from Shack–Hartmann Slope and Scintillation Data. *Appl. Opt.* **60** (2021)
33. Schroeder, D.J.: Adaptive Optics: An Introduction. In: *Astronomical Optics*, chap. 16, pp. 409–424. Elsevier (2000)
34. Schwartzman, A., Alterman, M., Zamir, R., Schechner, Y.Y.: Turbulence-Induced 2D Correlated Image Distortion. In: IEEE ICCP. pp. 1–13 (2017)
35. Sde-Chen, Y., Schechner, Y.Y., Holodovsky, V., Eytan, E.: 3DeepCT: Learning Volumetric Scattering Tomography of Clouds. In: Proc. ICCV (2021)
36. Sheinin, M., Schechner, Y.Y., Kutulakos, K.N.: Computational Imaging on the Electric Grid. In: Proc. IEEE CVPR (2017)
37. Shepherd, H.W., Osborn, J., Wilson, R.W., Butterley, T., Avila, R., Dhillon, V.S., Morris, T.J.: Stereo-SCIDAR: Optical Turbulence Profiling with High Sensitivity using a Modified SCIDAR Instrument. *MNRAS* **437**(4) (2014)
38. Smith, F.G.: The Infrared & Electro-Optical Systems Handbook: Volume 2 Atmospheric Propagation of Radiation, vol. 2. Infrared information and analysis center ann arbor mi (1993)
39. Storer, L.N., Williams, P.D., Gill, P.G.: Aviation Turbulence: Dynamics, Forecasting, and Response to Climate Change. *Pure and Applied Geophysics* (2019)
40. Thomas, H.E., Prata, A.J.: Computer Vision for Improved Estimates of SO<sub>2</sub> Emission Rates and Plume Dynamics. *IJRS* (2018)
41. Tian, Y., Narasimhan, S., Vannevel, A.: Depth from optical turbulence. In: Proc. IEEE CVPR (2012)
42. Toselli, I., Gladysz, S., Filimonov, G.: Scintillation Analysis of LIDAR Systems Operating in Weak-to-Strong Non-Kolmogorov Turbulence: Unresolved Target Case. *JARS* **12**(04), 1 (2018)
43. Venet, B.P.: Optical Scintillometry Over a Long Elevated Horizontal Path. *Airborne Laser Advanced Technology* **3381**(September 1998) (1998)
44. Vorontsov, A.M., Vorontsov, M.A., Filimonov, G.A., Polnau, E.: Atmospheric Turbulence Study with Deep Machine Learning of Intensity Scintillation Patterns. *Applied Sciences* (2020)



45. Ward, H.C.: Scintillometry in Urban and Complex Environments: A Review. *Measurement Science and Technology* (2017)
46. Wilcox, C.C., Santiago, F., Martinez, T., Judd, K.P., Restaino, S.R.: Horizontal Atmospheric Turbulence, Beam Propagation, and Modeling. *Micro- and Nanotechnology Sensors, Systems, and Applications IX* (2017)
47. Wu, C., Paulson, D., Iersel, M.V., Coffaro, J., Beason, M., Smith, C., Crabbs, R.F., Phillips, R., Andrews, L.: Near Ground Surface Turbulence Measurements and Validation: a Comparison Between Different Systems. In: *Laser Communication and Propagation through the Atmosphere and Oceans VII*. SPIE (2018)
48. Wu, C., Ko, J., Coffaro, J., Paulson, D.A., Rzasa, J.R., Andrews, L.C., Phillips, R.L., Crabbs, R., Davis, C.C.: Using Turbulence Scintillation to Assist Object Ranging From a Single Camera Viewpoint. *Applied Optics* **57**(9), 2177 (2018)
49. Yasarla, R., Patel, V.M.: Learning to Restore Images Degraded by Atmospheric Turbulence Using Uncertainty. In: *IEEE ICIP*. IEEE (2021)
50. Yi-Ting Tu, J.: Ray Optics Simulation. [ricktu288.github.io/ray-optics/](https://github.com/rickt288/ray-optics/)

# Tomography of Turbulence Strength Based on Scintillation Imaging Supplementary Material

Nir Shaul  and Yoav Y. Schechner 

Viterbi Faculty of Electrical and Computers Eng.,  
Technion - Israel Institute of Technology, Haifa, Israel  
nir.shaul@gmail.com , yoav@ee.technion.ac.il

**Abstract.** This is a supplementary document to the main manuscript. This document provides a detailed theoretical explanation and an illustration of the *seeing* effect, as a comparison to the scintillation effect. We also attach a video sample of the acquired data from the field experiment conducted in 02/02/2022. Additionally, we provide more simulated results.

## 1 Outline

This supplementary document contains four sections. Sec. 2 gives another intuition for the phenomenon of *seeing* and its path integral characteristics. In Sec. 3, we explain the scenario in the attached video, sampled during the outdoor experiment. Sec. 4 provides additional results of the simulated scintillation formation signal.

## 2 Modeling the Seeing Effect

According to Sec. 2 of the main manuscript, one of the turbulence visual effects is termed *seeing*. In this effect, random refraction perturbs the angle of arrival (AOA) of a ray from an object to the camera. Thus, the LOS of each pixel wiggles, creating spatiotemporal geometric distortions in image sequences. For an object at distance  $L$  and a camera having a lens aperture diameter  $D$ , the AOA of a line of sight (LOS) has variance given by Eqs. (3,4) of the main manuscript. The contribution is maximal by a turbulent air parcel right near the camera lens.

Here we provide an intuitive illustration of how a turbulent medium creates seeing, in a pinhole camera observing a single isotropic point source. Consider a very simplified case, where an air parcel has a shape of a prism, and its refractive index is slightly higher than that of calm steady air. Then, the air parcel acts as a refracting medium (Fig.1 herein). This effect yields a first order perturbation of the AOA.

If the air parcel is adjacent to the isotropic point source ( $z = 0$ ), then it has a negligible effect on the AOA at the camera. As a result, no matter what is the

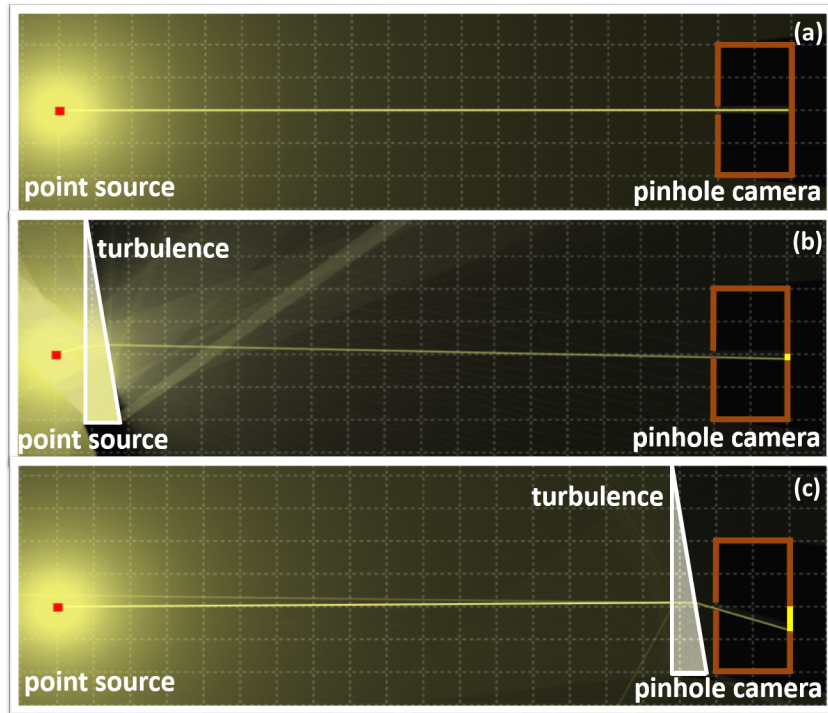


**Fig. 1.** Ray tracing simulation, illustrating the turbulence *seeing* phenomenon using a thin prism and a pinhole camera. The turbulence AOA influence is minor, when the turbulence is located close to the source (b). The influence becomes major when the turbulence is located near the camera pinhole (c). Based on the ray-tracing simulator of [1].

random refractive index of the air parcel, it does not change the AOA in this case. However, if the air parcel is adjacent to the pinhole camera, ( $z = L$ ), it has a significant effect: the light ray which enters the pinhole can have a high AOA bias. Because the air-parcel has a random refractive index, the perturbation of the AOA is random, and in this case, having high values of  $\sigma_{AOA}^2$ . This leads to observed seeing.

### 3 Scintillating Lights Capturing

We make the the raw data, codes and system design of the field experiment publicly available in: <https://github.com/nirshaul/ScintillationTomography> We also attach a video sampled during the outdoor experiment. The video file includes 50 frames of scintillating lights in the scene, as captured in viewpoint 4. The video attached is a compressed version (95%, for file upload limits) of the operational capture. In Fig. 2 herein, we can notice the same scene of the operational video, as captured in the preliminary capture. In this scene we can



**Fig. 2.** Preliminary capture of the scene in the attached video file. Taken from view-point 4, angle 20.

notice a complex urban region composed of an industrial foreground, rural and residential background areas. Notice the strong scintillation of lights in the upper part of the image (background), where LOSs, cross through the industrial area.

## 4 Model Simulation

The scintillation model described in Sec. 3 of the main paper is influenced by multiple imaging parameters. In this section we show how some imaging parameters influence the scintillation signal, in terms of the scintillation index estimation relative error:

$$\epsilon_{\text{err}} = \frac{|\hat{\sigma}_I^2 - \sigma_I^2|}{\sigma_I^2}. \quad (1)$$

Settings as mentioned in Sec. 5 of the main manuscript are used here. Each pixel has full-well of 3000 photoelectrons and 8-bit quantization, i.e., the expected number of photoelectrons per graylevel is 11.8. Using these specifications, each noisy measurement is drawn from a Poisson distribution of photoelectrons, and then quantized. A sequence of 1000 frames was used for analysis. From this sequence, we estimated  $\hat{\sigma}_I^2$ . We used a spatial gaussian (a kernel of  $50 \times 50$  pixels, having standard deviation  $\sigma_g = 5$  pixels), as a captured light source, i.e.

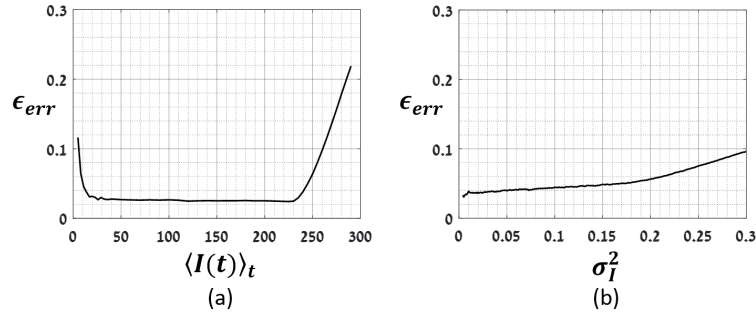


**Fig. 3.** (a)  $\epsilon_{err}$  as function of  $\langle I(t) \rangle_t$  (b)  $\epsilon_{err}$  as function of  $\sigma_I^2$ .

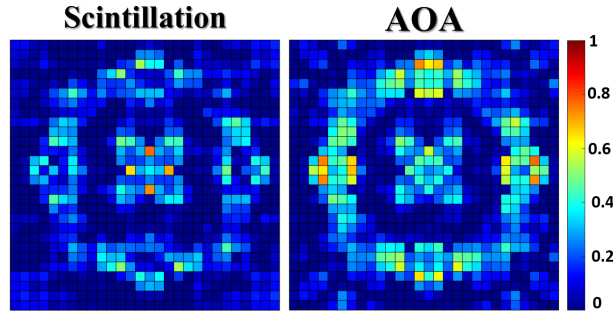


**Fig. 4.** Ratio of TS Reconstruction error relative to the ground truth, by scintillation (left) and by AOA (right).

a blob in an image. We compensated the photon noise variance according to Eq.(12) of the main manuscript.

We studied how varying  $\sigma_I^2$  between 0.001 to 0.3 (typical values for very weak to weak scintillation) affect the estimation results (Fig. 3b herein). We can see that  $\epsilon_{err}$  increases with the scintillation index.

In addition, we studied how the temporal mean value of a scintillating blob, i.e.  $\langle I(t) \rangle_t$ , affects  $\epsilon_{err}$  (Fig. 3a herein). As expected, for high values of  $\langle I(t) \rangle_t$ , the signal clips due to saturation of the sensor. So, the estimation degrades (high  $\epsilon_{err}$ ). On the other hand, in low values of  $\langle I(t) \rangle_t$ , the acquisition suffers from a low signal to noise ratio, which also degrades the estimation.

We also studied how  $\sigma_g$  (spatial standard deviation of the captured source) affects  $\epsilon_{err}$ . We examined the range  $0.5 \leq \sigma_g \leq 30$ , and noticed that this parameter has no influence on  $\epsilon_{err}$ .

In Fig. 4 herein, we add an additional visualization of the simulated experiment of Fig. 6 of the main manuscript. The figure shows the ratio of the turbulence-strength (TS) error, to the ground-truth. Notice the error is major in AOA reconstruction.

## References

1. Yi-Ting Tu, J.: Ray Optics Simulation. [ricktu288.github.io/ray-optics/](https://ricktu288.github.io/ray-optics/)